nature astronomy

SUPPLEMENTARY INFORMATION

https://doi.org/10.1038/s41550-019-0800-5

In the format provided by the authors and unedited.

# A sub-Neptune exoplanet with a low-metallicity methane-depleted atmosphere and Mie-scattering clouds

**Björn Benneke[1]*, Heather A. Knutson[2], Joshua Lothringer[3], Ian J.M. Crossfield[4], Julianne I. Moses[5], Caroline Morley[6], Laura Kreidberg[7], Benjamin J. Fulton[2], Diana Dragomir[4], Andrew W. Howard[8], Ian Wong[9], Jean-Michel Désert[10], Peter R. McCullough[11], Eliza M.-R. Kempton[12,13], Jonathan Fortney[14], Ronald Gilliland[15], Drake Deming[12] and Joshua Kammer[16]**

[1]Department of Physics and Institute for Research on Exoplanets, Université de Montréal, Montréal, Quebec, Canada. [2]Division of Geological and Planetary Sciences, California Institute of Technology, Pasadena, CA, USA. [3]Lunar and Planetary Laboratory, University of Arizona, Tucson, AZ, USA. [4]Department of Physics and Kavli Institute of Astronomy, Massachusetts Institute of Technology, Cambridge, MA, USA. [5]Space Science Institute, Boulder, CO, USA. [6]Department of Astronomy, University of Texas, Austin, TX, USA. [7]Department of Astronomy, Harvard University, Cambridge, MA, USA. [8]Department of Astronomy, California Institute of Technology, Pasadena, CA, USA. [9]Department of Earth, Atmospheric, and Planetary Sciences, Massachusetts Institute of Technology, Cambridge, MA, USA. [10]Anton Pannekoek Institute for Astronomy, University of Amsterdam, Amsterdam, The Netherlands. [11]Department of Physics and Astronomy, Johns Hopkins University, Baltimore, MD, USA. [12]Department of Astronomy, University of Maryland, College Park, MD, USA. [13]Department of Physics, Grinnell College, Grinnell, IA, USA. [14]Department of Astronomy, University of California, Santa Cruz, CA, USA. [15]Space Telescope Science Institute, Baltimore, MD, USA. [16]Southwest Research Institute, San Antonio, TX, USA. *e-mail: bbenneke@astro.umontreal.ca

Supplementary Information

# A Sub-Neptune Exoplanet with a Low-Metallicity Methane-Depleted Atmosphere and Mie-Scattering Clouds

BJÖRN BENNEKE[1], HEATHER A. KNUTSON[2], JOSHUA LOTHRINGER[3], IAN CROSSFIELD[4], JULIANNE MOSES[5], CAROLINE MORLEY[6], LAURA KREIDBERG[7], BJ FULTON[2], DIANA DRAGOMIR[4,17], ANDREW HOWARD[8], IAN WONG[9], JEAN-MICHEL DÉSERT[10], P.R. MCCULLOUGH[11], ELIZA M.-R. KEMPTON[12,13,], JONATHAN FORTNEY[14], RONALD GILLILAND[15], DRAKE DEMING[12], JOSHUA KAMMER[16]

[18] Department of Physics and Institute for Research on Exoplanets, Université de Montréal, Montréal, QC, Canada
[19] Division of Geological and Planetary Sciences, California Institute of Technology, Pasadena, CA 91125, USA
[20] Lunar & Planetary Laboratory, University of Arizona, 1629 E. University Boulevard., Tucson, AZ, USA
[21] Department of Physics and Kavli Institute of Astronomy, Massachusetts Institute of Technology, 77 Massachusetts Ave, Cambridge, MA, 02139, USA
[22] Space Science Institute, 4750 Walnut Street, Suite 205, Boulder, CO 80301, USA
[23] Department of Astronomy, University of Texas, Austin, TX 78712, USA
[24] Department of Astronomy, Harvard University, 60 Garden Street, Cambridge, MA 02138, USA
[25] Department of Astronomy, California Institute of Technology, Pasadena, CA 91125, USA
[26] Department of Earth, Atmospheric, and Planetary Sciences, Massachusetts Institute of Technology, 77 Massachusetts Ave, Cambridge, MA, 02139, USA
[27] Anton Pannekoek Institute for Astronomy, University of Amsterdam, 1090 GE Amsterdam, The Netherlands
[28] Department of Physics and Astronomy, Johns Hopkins University, Baltimore, MD 21218, USA
[29] Department of Astronomy, University of Maryland, College Park, MD 20742, USA
[30] Department of Physics, Grinnell College, 1116 8th Avenue, Grinnell, IA 50112, USA
[31] Department of Astronomy, University of California, Santa Cruz, CA 95064, USA
[32] Space Telescope Science Institute, 3700 San Martin Dr., Baltimore, MD 21218, USA
[33] Southwest Research Institute, San Antonio TX, USA
[34] NASA Hubble Fellow

771

| Instrument | Filter/Grism | Transit/Eclipse | Wavelength [μm] | UT Start Date |
|---|---|---|---|---|
| HST/STIS | G750L | Transits | 0.55 – 1.0 | 2015 Feb 07<br>2015 May 12<br>2016 Apr 03 |
| HST/WFC3 | G141 | Transits | 1.1 – 1.7 | 2015 Jan 28<br>2015 Mar 13<br>2015 Oct 22 |
| Spitzer/IRAC | Channel 1 | Transits | 3.0 – 4.0 | 2012 Dec 22<br>2017 Jan 25<br>2017 Feb 20 |
| Spitzer/IRAC | Channel 2 | Transits | 4.0 – 5.0 | 2012 Jun 11<br>2012 Jun 15<br>2013 Jan 01 |
| Spitzer/IRAC | Channel 1 | Eclipse | 3.0 – 4.0 | 2014 Jan 15<br>2014 Jan 28<br>2014 Jun 14<br>2014 Jun 24<br>2015 Jan 30<br>2015 Feb 06<br>2015 Feb 09<br>2015 Feb 12<br>2015 Jun 19<br>2015 Jul 19 |
| Spitzer/IRAC | Channel 2 | Eclipse | 4.0 – 5.0 | 2014 Jan 21<br>2014 Feb 4<br>2014 Jun 21<br>2014 Jul 10<br>2015 Jan 10<br>2015 Jan 13<br>2015 Jan 17<br>2015 Jan 20<br>2015 Jan 23<br>2015 Jan 27 |

772 Supplementary Table 1: Summary of presented transit and eclipse observation of GJ 3470b.

773

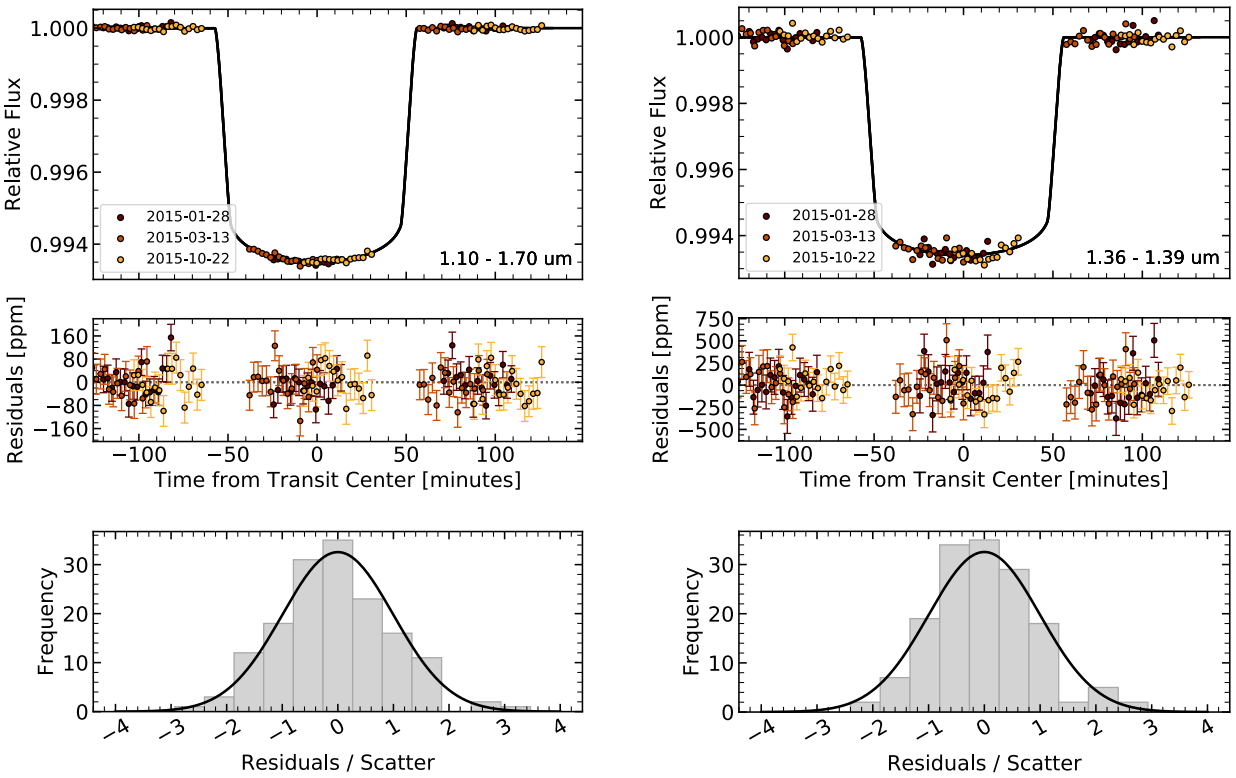


Supplementary Figure 1: White light curve fit (left) and a typical spectral light curve fit (right) from the joint analysis of the three WFC3 transit observations of GJ 3470b. The top panel shows the best fitting model light curves (black curve), overlaid with the systematics-corrected data (circles). Residuals from the light curve fits are shown in the middle panels. All corrected WFC3 light curve fits are free of obvious systematics. The bottom panels shows a histogram of the residuals normalized by the fitted photometric scatter parameter for each respective transit. The residuals follow the expected Gaussian distribution for photon noise limited observations.

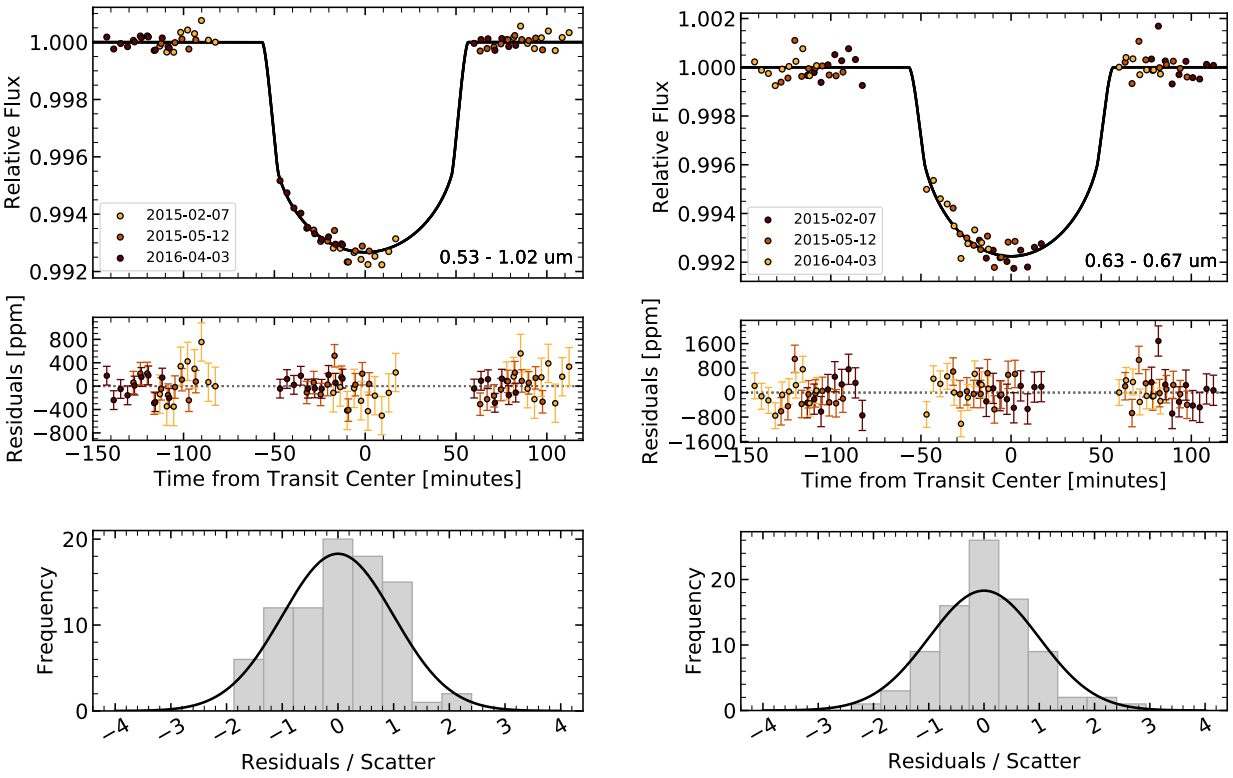


Supplementary Figure 2: White light curve fit (left) and a typical spectral light curve fit (right) from the joint analysis of the three STIS transit observations of GJ 3470b. The top panel shows the best fitting model light curves (black curve), overlaid with the systematics-corrected data (circles). Residuals from the light curve fits are shown in the middle panels. The bottom panels shows a histogram of the residuals normalized by the fitted photometric scatter parameter for each respective transit.

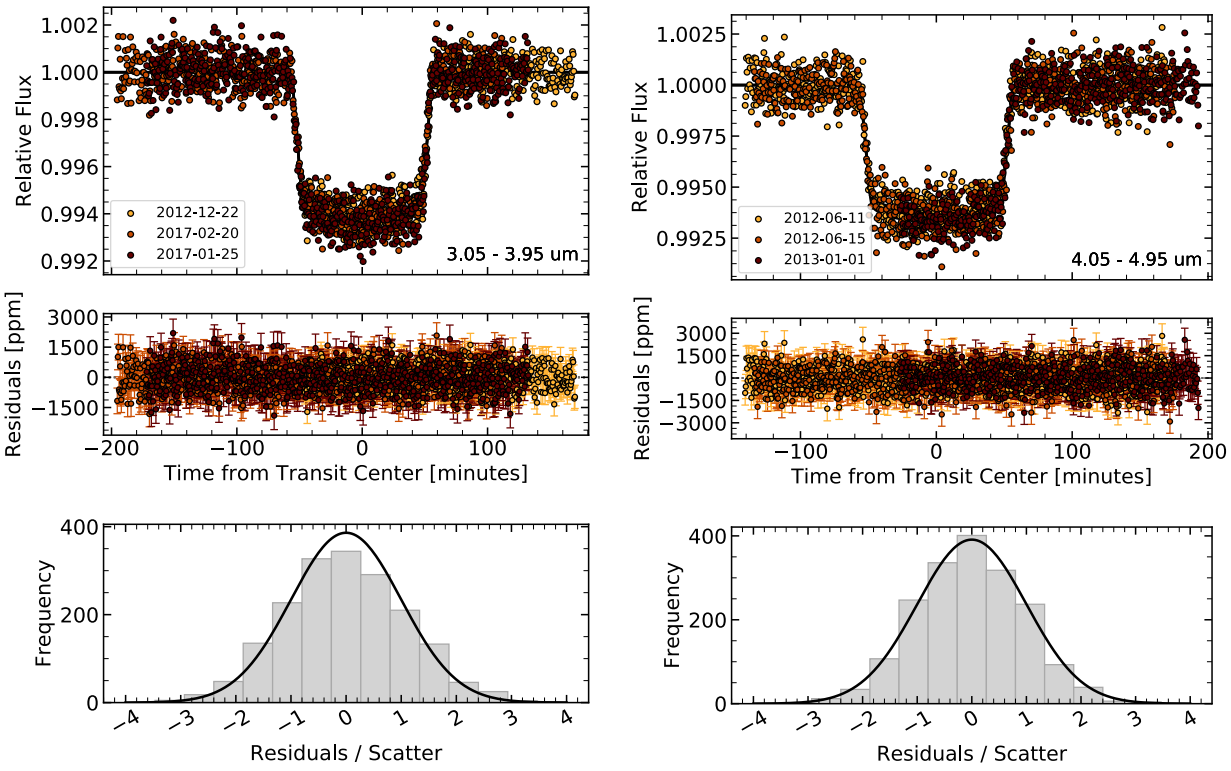


Supplementary Figure 3: Spitzer light curve fits of three 3.6μm transit (left) and three 4.5μm transits (right). The top panel shows the best fitting model light curves (black curve), overlaid with the systematics-corrected data (colored circles). Residuals from the light curve fits are shown in the middle panels. All corrected Spitzer light curve fits are free of obvious systematics. The bottom panels shows a histogram of the residuals normalized by the fitted photometric scatter parameter for each respective transit. The residuals follow the expected Gaussian distribution for photon noise limited observations.

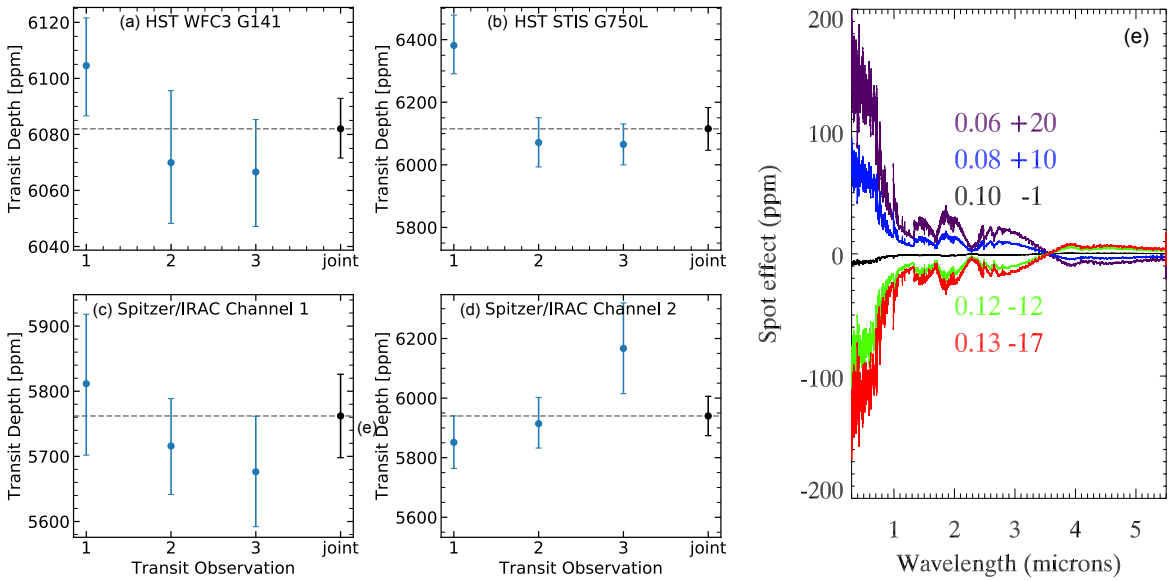


Supplementary Figure 4: (Left and center) Repeatability of transit depth measurements. Panels (a)-(d) show the transit depths from the individual transit fits (blue) and joint fit (black) for HST/WFC3 (a), HST/STIS (b), Spitzer/IRAC 3.6µm (c) and Spitzer/IRAC 4.5µm (d). The individual transit depth measurement are consistent over time within their statistical uncertainties and with the joint fit. (Right) Modeled spectra showing the potential effects of star spots on the apparent transmission spectrum. Colored curves indicate the effect for a fraction f of 0.06 (purple), 0.08 (blue), 0.1 (black), 0.12 (green) and 0.13 (red) as discussed in the Methods Section. The second value indicates the increase in the apparent transit depth within the WFC3 bandpass in parts-per-million (p.p.m).

| Visit # | λ (μm) | UT Start Date | $t_{trim}$ (hr)[a] | $n_{bin}$ [a] | Varying aperture? | Noise Pixel Scaling | Average $r_{phot}$ [a] | Bkd (%)[b] |
|---|---|---|---|---|---|---|---|---|
| 1 | 3.6 | UT 2012 Dec 22 | 0.5 | 128 | no | | 2.7 | 0.91 |
| 2 | 3.6 | UT 2017 Jan 25 | 0.75 | 64 | no | | 2.8 | 1.01 |
| 3 | 3.6 | UT 2017 Feb 20 | 0.75 | 128 | no | | 2.5 | 1.04 |
| 1 | 4.5 | UT 2012 Jun 11 | 0.75 | 128 | no | | 2.6 | 0.29 |
| 2 | 4.5 | UT 2012 Jun 15 | 0.75 | 64 | no | | 2.7 | 0.32 |
| 3 | 4.5 | UT 2013 Jan 01 | 0.5 | 64 | no | | 2.7 | 0.35 |
| 1 | 3.6 | UT 2014 Jan 15 | 1.5 | 64 | yes | 1.1x scaling | 2.6 | 0.92 |
| 2 | 3.6 | UT 2014 Jan 28 | 0.5 | 192 | no | | 2.3 | 0.82 |
| 3 | 3.6 | UT 2014 Jun 14 | 0.5 | 128 | no | | 2.2 | 0.65 |
| 4 | 3.6 | UT 2014 Jun 24 | 1.5 | 128 | yes | 0.9x scaling | 2.5 | 0.67 |
| 5 | 3.6 | UT 2015 Jan 30 | 1.5 | 64 | no | | 2.2 | 0.69 |
| 6 | 3.6 | UT 2015 Feb 06 | 1.5 | 128 | yes | 1.2x scaling | 3.0 | 1.26 |
| 7 | 3.6 | UT 2015 Feb 09 | 0.5 | 192 | no | | 2.7 | 1.16 |
| 8 | 3.6 | UT 2015 Feb 12 | 1.5 | 192 | no | | 2.3 | 0.91 |
| 9 | 3.6 | UT 2015 Jun 19 | 0.5 | 128 | no | | 2.2 | 0.71 |
| 10 | 3.6 | UT 2015 Jul 19 | 0.5 | 192 | no | | 2.3 | 0.80 |
| 1 | 4.5 | UT 2014 Jan 21 | 1.5 | 64 | no | | 2.5 | 0.30 |
| 2 | 4.5 | UT 2014 Feb 04 | 1.0 | 128 | no | | 2.3 | 0.22 |
| 3 | 4.5 | UT 2014 Jun 21 | 1.0 | 64 | no | | 2.3 | 0.10 |
| 4 | 4.5 | UT 2014 Jul 10 | 1.0 | 64 | no | | 2.3 | 0.29 |
| 5 | 4.5 | UT 2015 Jan 10 | 1.5 | 64 | no | | 2.1 | 0.37 |
| 6 | 4.5 | UT 2015 Jan 13 | 1.0 | 128 | no | | 2.3 | 0.34 |
| 7 | 4.5 | UT 2015 Jan 17 | 1.5 | 64 | no | | 2.1 | 0.30 |
| 8 | 4.5 | UT 2015 Jan 20 | 1.0 | 128 | no | | 2.4 | 0.35 |
| 9 | 4.5 | UT 2015 Jan 23 | 0.5 | 128 | no | | 2.3 | 0.28 |
| 10 | 4.5 | UT 2015 Jan 27 | 1.5 | 64 | no | | 2.7 | 0.34 |

Supplementary Table 2: Summary of *Spitzer* transit observations (top) and eclipse observation (bottom)

[a] $t_{trim}$ is the amount of time trimmed from the start of each time series, $n_{bin}$ is the bin size used in the photometric fits, and $r_{phot}$ is the radius of the photometric aperture in pixels.

[b] Relative sky background contribution to the total flux in the selected aperture

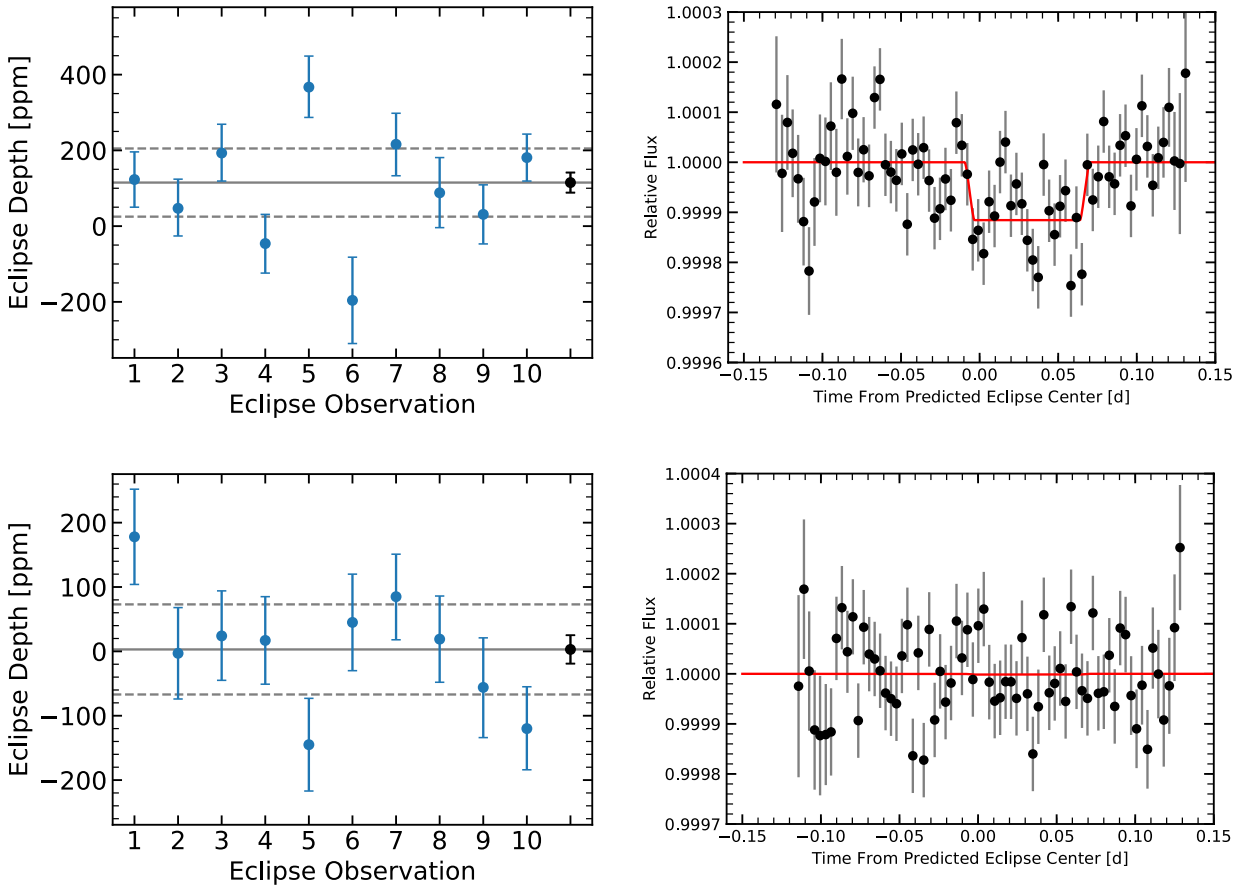


Supplementary Figure 5: Spitzer/IRAC secondary eclipse observations of GJ 3470b at 3.6 μm (top) and 4.5 μm (bottom). The left panels show the estimates of the eclipse depths for each of the ten individual eclipse observations (blue) and the global fit (black). Typical ±1σ uncertainties for individual eclipse fits are shown by gray dashed horizontal lines around the global fit value. The ten individual measurements are randomly distributed around the global fit. Consistent with the uncertainties, 6 of 10 and 7 of 10 data points are within the 68% confidence interval for the observations at 3.6 and 4.5 μm, respectively. The right panels shows the best fitting model light curves (red curve) from the global fit, overlaid with the systematics-corrected Spitzer data from all ten eclipse observations (black). The eclipse is slightly offset relative to the estimated eclipse time for a perfectly circular orbit. This is consistent with fits to the radial velocity data of GJ 3470b, which independently confirm a small but non-zero eccentricity (Kosiarek et al. 2018).

| Instrument/Grism | Wavelength [μm] | | | Depth [ppm] | +1σ [ppm] | -1σ [ppm] |
|---|---|---|---|---|---|---|
| **Transit:** | | | | | | |
| HST STIS G750L | 0.528 | – | 0.577 | 5912 | 178 | 192 |
| HST STIS G750L | 0.577 | – | 0.626 | 6135 | 104 | 104 |
| HST STIS G750L | 0.626 | – | 0.674 | 5999 | 89 | 94 |
| HST STIS G750L | 0.674 | – | 0.723 | 5945 | 91 | 91 |
| HST STIS G750L | 0.723 | – | 0.772 | 5937 | 98 | 107 |
| HST STIS G750L | 0.772 | – | 0.821 | 6215 | 85 | 86 |
| HST STIS G750L | 0.821 | – | 0.870 | 6093 | 108 | 110 |
| HST STIS G750L | 0.870 | – | 0.919 | 6098 | 113 | 119 |
| HST WFC3 G141 | 1.120 | – | 1.150 | 6101 | 34 | 35 |
| HST WFC3 G141 | 1.150 | – | 1.180 | 6050 | 37 | 34 |
| HST WFC3 G141 | 1.180 | – | 1.210 | 6077 | 33 | 34 |
| HST WFC3 G141 | 1.210 | – | 1.240 | 6035 | 31 | 32 |
| HST WFC3 G141 | 1.240 | – | 1.270 | 6126 | 34 | 31 |
| HST WFC3 G141 | 1.270 | – | 1.300 | 6082 | 31 | 29 |
| HST WFC3 G141 | 1.300 | – | 1.330 | 6055 | 29 | 29 |
| HST WFC3 G141 | 1.330 | – | 1.360 | 6196 | 26 | 28 |
| HST WFC3 G141 | 1.360 | – | 1.390 | 6178 | 31 | 30 |
| HST WFC3 G141 | 1.390 | – | 1.420 | 6111 | 32 | 32 |
| HST WFC3 G141 | 1.420 | – | 1.450 | 6127 | 29 | 31 |
| HST WFC3 G141 | 1.450 | – | 1.480 | 6136 | 31 | 32 |
| HST WFC3 G141 | 1.480 | – | 1.510 | 6124 | 32 | 31 |
| HST WFC3 G141 | 1.510 | – | 1.540 | 6079 | 26 | 29 |
| HST WFC3 G141 | 1.540 | – | 1.570 | 6121 | 31 | 32 |
| HST WFC3 G141 | 1.570 | – | 1.600 | 6057 | 34 | 30 |
| HST WFC3 G141 | 1.600 | – | 1.630 | 6059 | 33 | 35 |
| HST WFC3 G141 | 1.630 | – | 1.660 | 6061 | 32 | 32 |
| Spitzer/IRAC 3.6μm | 3.15 | – | 3.90 | 5763 | 64 | 65 |
| Spitzer/IRAC 4.5μm | 4.00 | – | 5.00 | 5941 | 60 | 66 |
| **Eclipse:** | | | | | | |
| Spitzer/IRAC 3.6μm | 3.15 | – | 3.90 | 115 | 27 | 26 |
| Spitzer/IRAC 4.5μm | 4.00 | – | 5.00 | 3 | 22 | 22 |

Supplementary Table 3: Transmission spectrum and eclipse depths

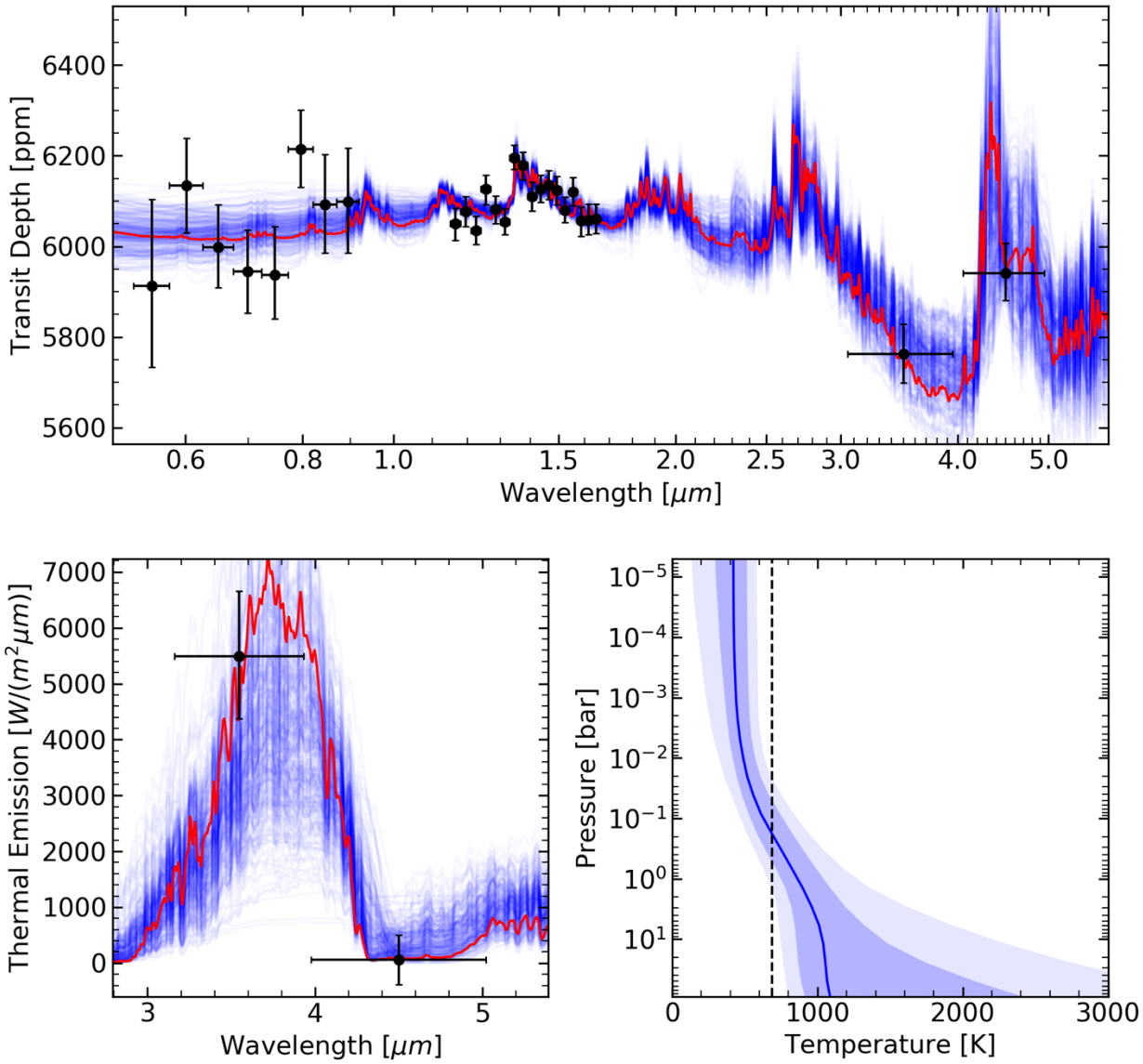


Supplementary Figure 6: Spectral fits and temperature profile constraints from the joint retrieval analysis of GJ 3470b's transit and eclipse data. The top and bottom left panels show the range of models fitting the observations (black) by depicting a random sample of 300 atmospheric models from the posterior distribution (thin blue curves). The best fitting model is shown as thick red curve. Consistent with the observed transit depth uncertainties, the models are tightly constrained within the precise *HST/WFC3* observations. At shorter and longer wavelengths, the *HST/STIS* and *Spitzer* observations allow for a slightly larger range of transit depths, mostly by slight changes in the cloud parameters as well as the CO and $CO_2$ abundances. The bottom right panel depicts the posterior constraints on the vertical temperature profile. The dark and light-blue shaded regions are the 1σ and 2σ spread in the temperature profiles, with the solid blue curve being the median temperature profile of all models in the posterior distribution. The equilibrium temperature for an planetary albedo of 0.1 is shown for comparison (dashed line).

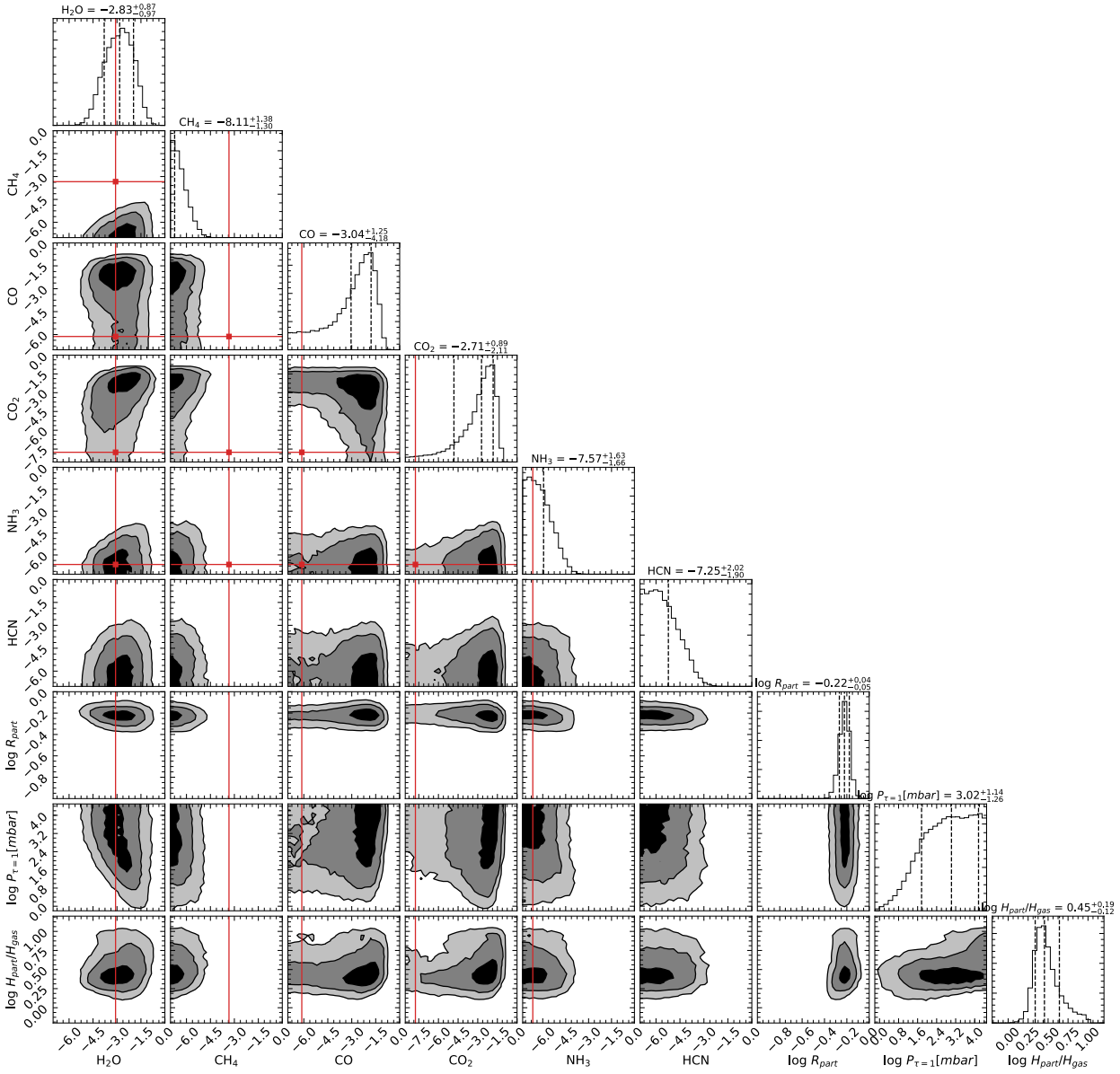


Supplementary Figure 7: Molecular abundance and cloud property constraints from the joint retrieval analysis of the transit and eclipse data. The top panels in each column show the 1D marginalized posterior distributions of the molecular abundances and cloud properties, with dashed vertical lines in the histograms indicating the marginalized 16th, 50th, and 84th percentiles. The subjacent 2D panels show the correlations among the gases and cloud properties, with the black, dark-gray, and light-gray regions corresponding to the 1σ (39.3%), 2σ (86.5%), and 3σ (98.9%) credible intervals. The vertical and horizontal red lines in each panel are the solar composition molecular abundances at 700 K and 0.1 bars, a representative photospheric temperature and pressure. The water mixing ratio is constrained to ±1 order of magnitude around 1 times solar. $CH_4$ and $NH_3$ are depleted. Note also the "elbow"-shaped correlation between CO and $CO_2$. This degeneracy arises because CO and $CO_2$ both absorb within the 4.5 μm Spitzer bandpass observed in transit and eclipse. Note that the retrieval included an additional 7 parameters for the vertical temperature structure and common-mode transit depth uncertainties which are not displayed here for clarity.

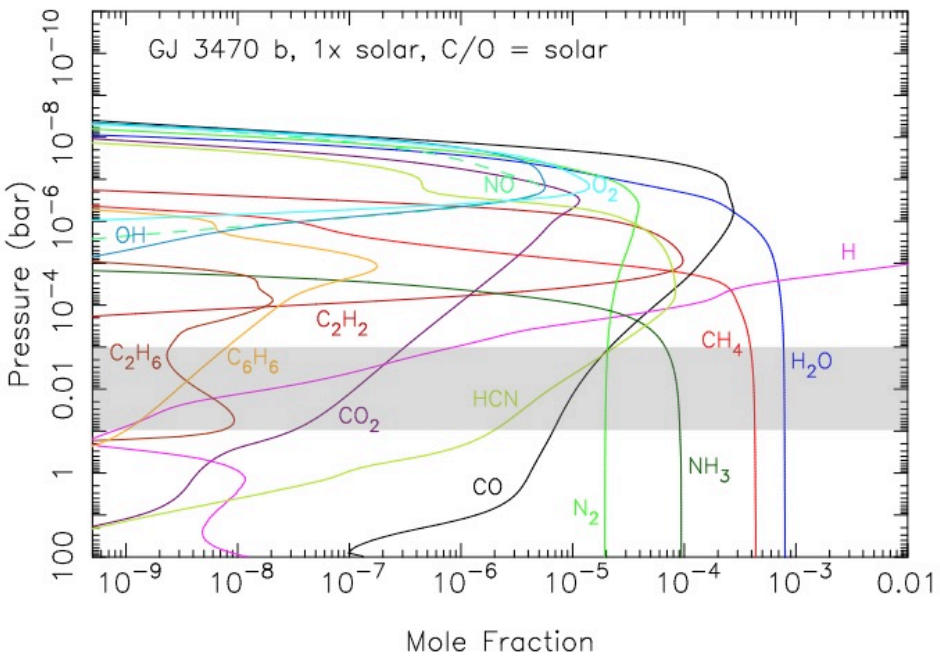


859

860 Supplementary Figure 8: Mixing-ratio profiles for several species of interest (as labeled) in our
861 kinetics/transport models for GJ 3470b, for solar atmospheric metallicity and a C/O ratio of 0.54. The
862 gray horizontal zone indicates pressure range to which our observations are most sensitive. The thermal
863 emission observations extend to slightly deeper levels as well. Water and methane abundance follow
864 mostly the equilibrium abundances, with photodissociation becoming relevant above approximately $10^{-5}$
865 bar, as previously also shown in a theoretical modeling investigation of the sub-Neptune GJ 1214b[15] and
866 GJ 436b[16,21]. Ammonia is expected to be abundant the photosphere due to quenching resulting from
867 vertical transport and the slow rate of reaction for the conversion to $N_2$ and $H_2$.

868

869

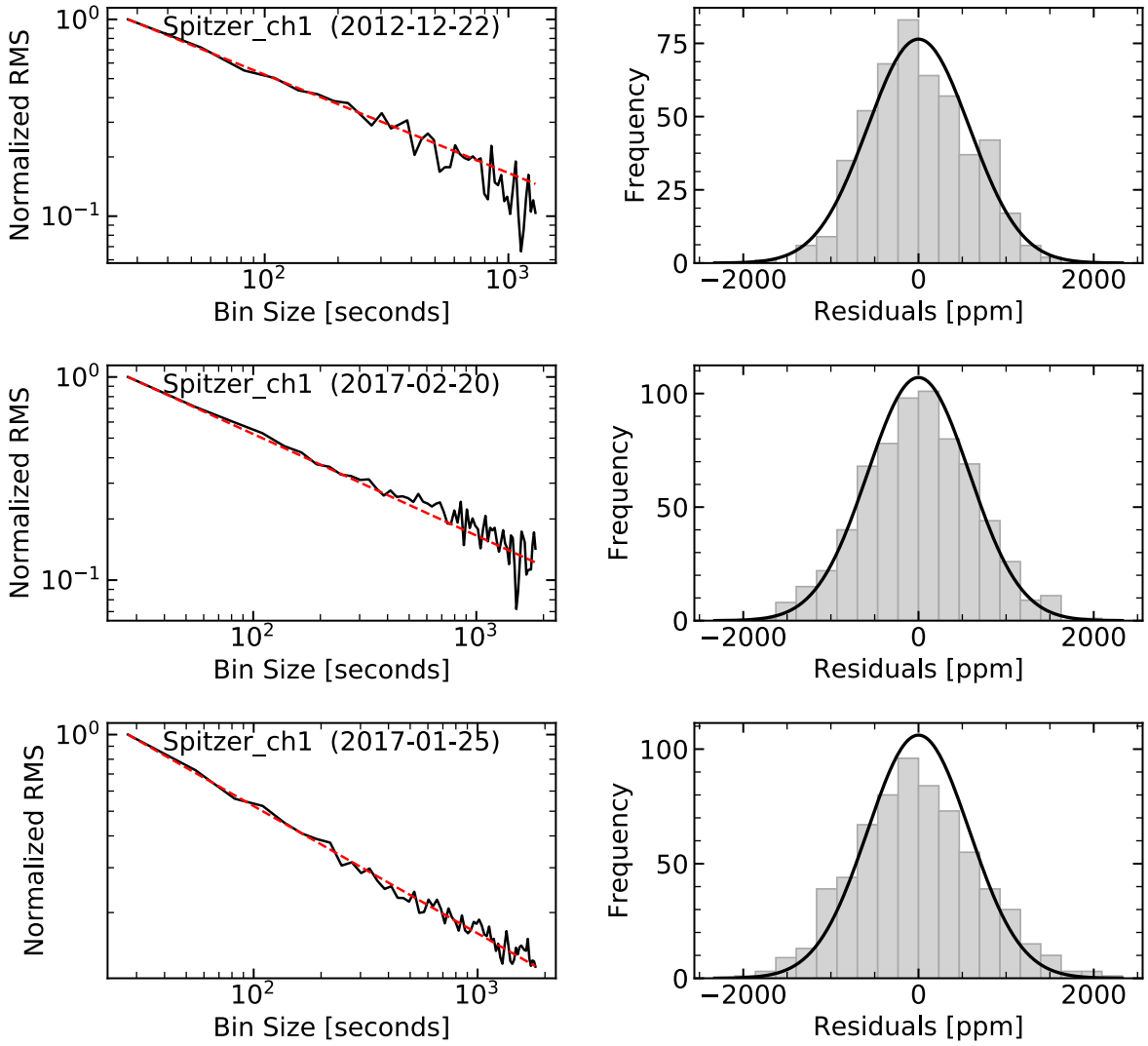


870

871 Supplementary Figure 9: Analysis of residuals from fitting the three Spitzer/IRAC 3.6um transits (top,
872 center, bottom). Left panels: Photometric scatter vs. the width of the binning interval for Spitzer data. The
873 root-mean-square error of the systematics-corrected Spitzer data (black) follows closely the theoretical
874 square-root scaling for uncorrelated white noise (red dashed line), even when binned all the way to 30
875 minute intervals. Right panels: Histogram of the residuals (grey bars) compared to a theoretical Gaussian
876 distribution with the width of the scatter parameter fitted as a nuisance parameter in the Bayesian analysis
877 (black curve). The residuals are consistent with the Gaussian distribution and the scatter parameter.

878

879

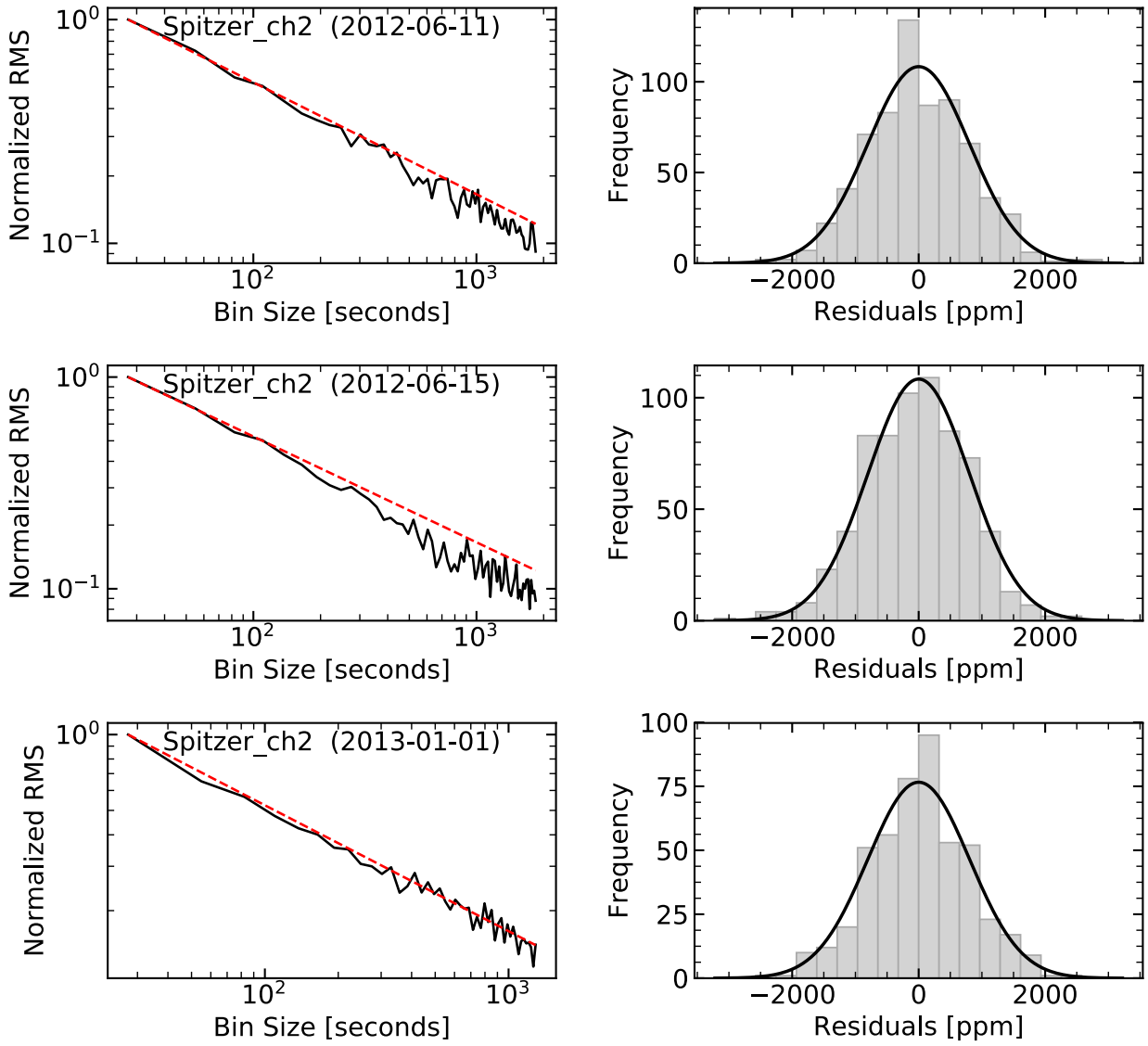


Supplementary Figure 10: Analysis of residuals from fitting the three Spitzer/IRAC 4.5um transits (top, center, bottom). Left panels: Photometric scatter vs. the width of the binning interval for Spitzer data. The root-mean-square error of the systematics-corrected Spitzer data (black) follows closely the theoretical square-root scaling for uncorrelated white noise (red dashed line), even when binned all the way to 30 minute intervals. Right panels: Histogram of the residuals (grey bars) compared to a theoretical Gaussian distribution with the width of the scatter parameter fitted as a nuisance parameter in the Bayesian analysis (black curve). The residuals are consistent with the Gaussian distribution and the scatter parameter.

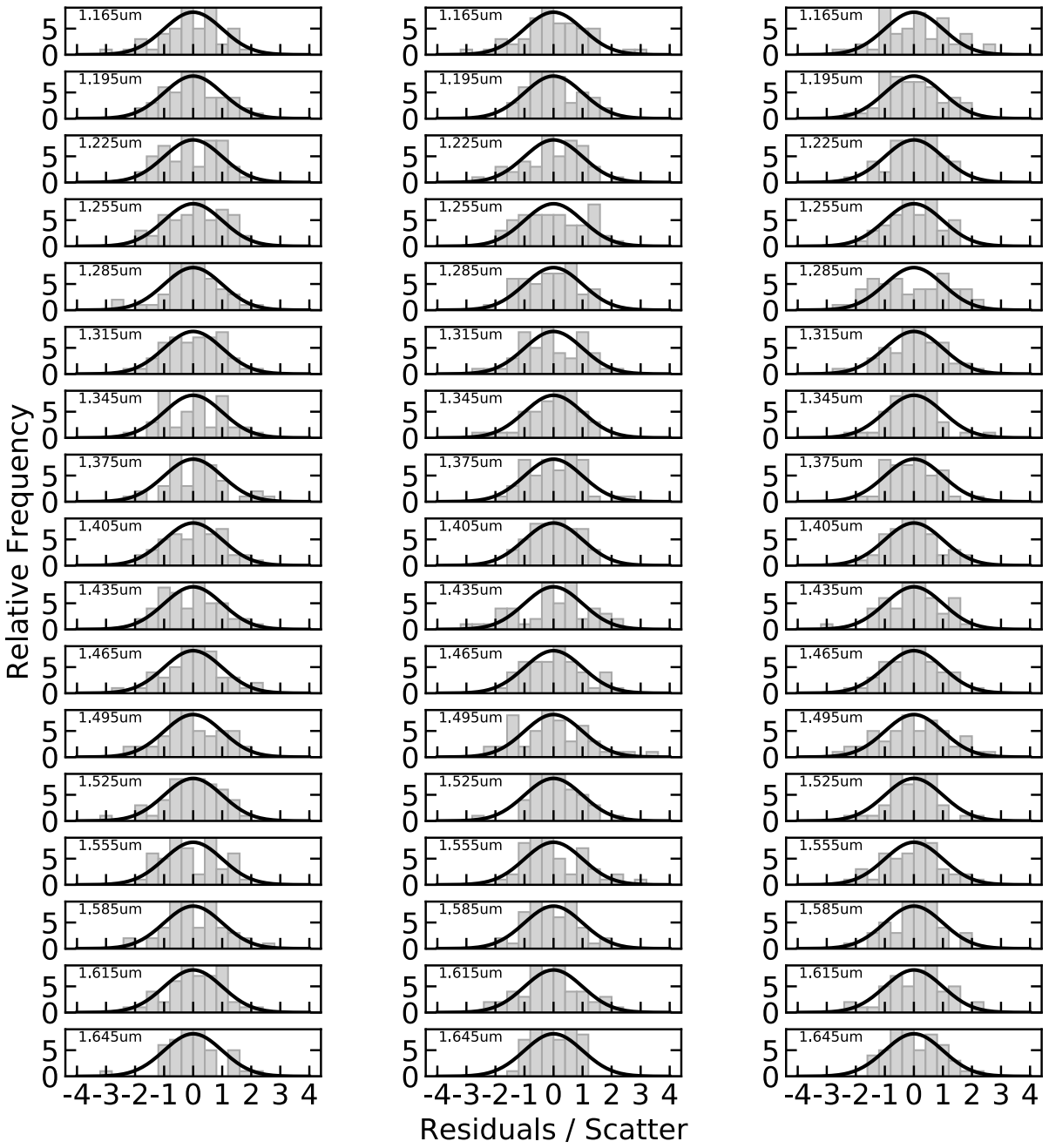


Supplementary Figure 11: Histograms of residuals from HST/WFC3 spectral light curve fits. This figure shows the histograms for each wavelength bin (rows) and each transit (columns) individually. Residuals are normalized by the fitted scatter parameter for the respectively wavelength bin and transit. The histogram of normalized residuals (gray bars) is compared to the normal distribution (black curve). Each histogram is made of only 51 data points leading to relatively poor sampling of each frequency distribution; however, no statistically significant deviation from the expected frequency distribution is observed. The agreement with the expected Gaussian distribution can be seen even better in the combined plot of all residuals shown in Supplementary Figure 12. WFC3 residuals are highly consistent with the Gaussian distribution and the fitted scatter parameter for each light curve.

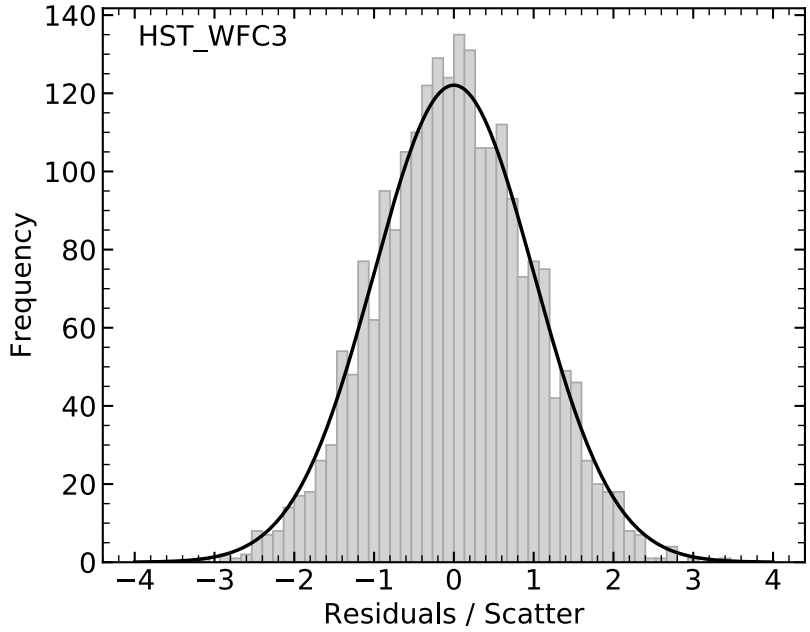


Supplementary Figure 12. Histograms of all residuals from WFC3 spectral light curve fits. This plot combines the residuals from all panels in Supplementary Figure 11 in order to increase the number of samples in the histogram. WFC3 residuals are highly consistent with the Gaussian distribution and the fitted scatter parameter for each light curve.

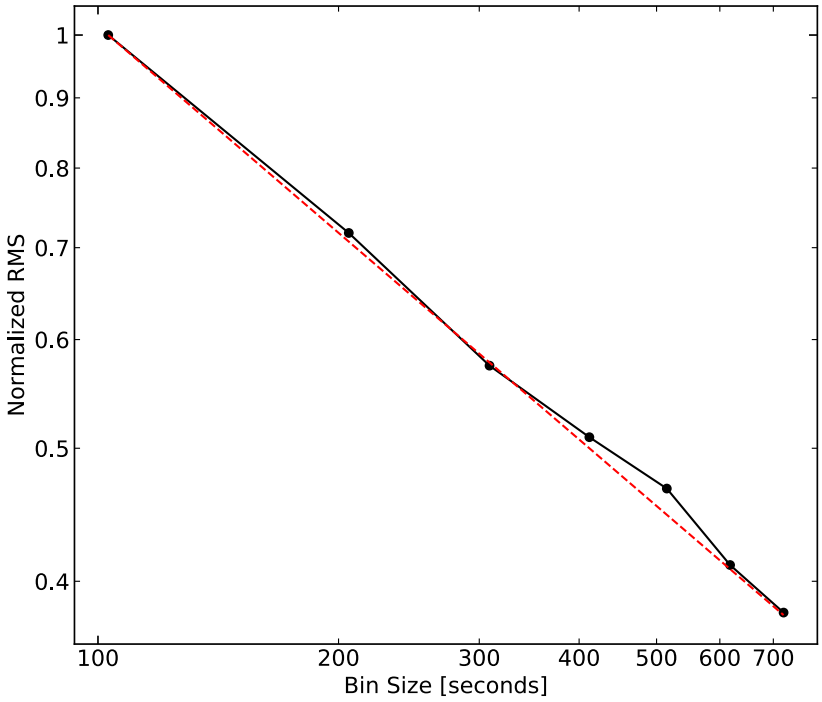


Supplementary Figure 13: Photometric scatter vs. the width of the time binning interval for all WFC3 spectroscopic light curves combined. The root-mean-square error of the systematics-corrected WFC3 data (black) follows closely the theoretical square-root scaling for uncorrelated white noise (red dashed line), even when binned all the way to 12 minute intervals. At this point only four data points are left per orbit. We conclude that time correlated noise is negligible.

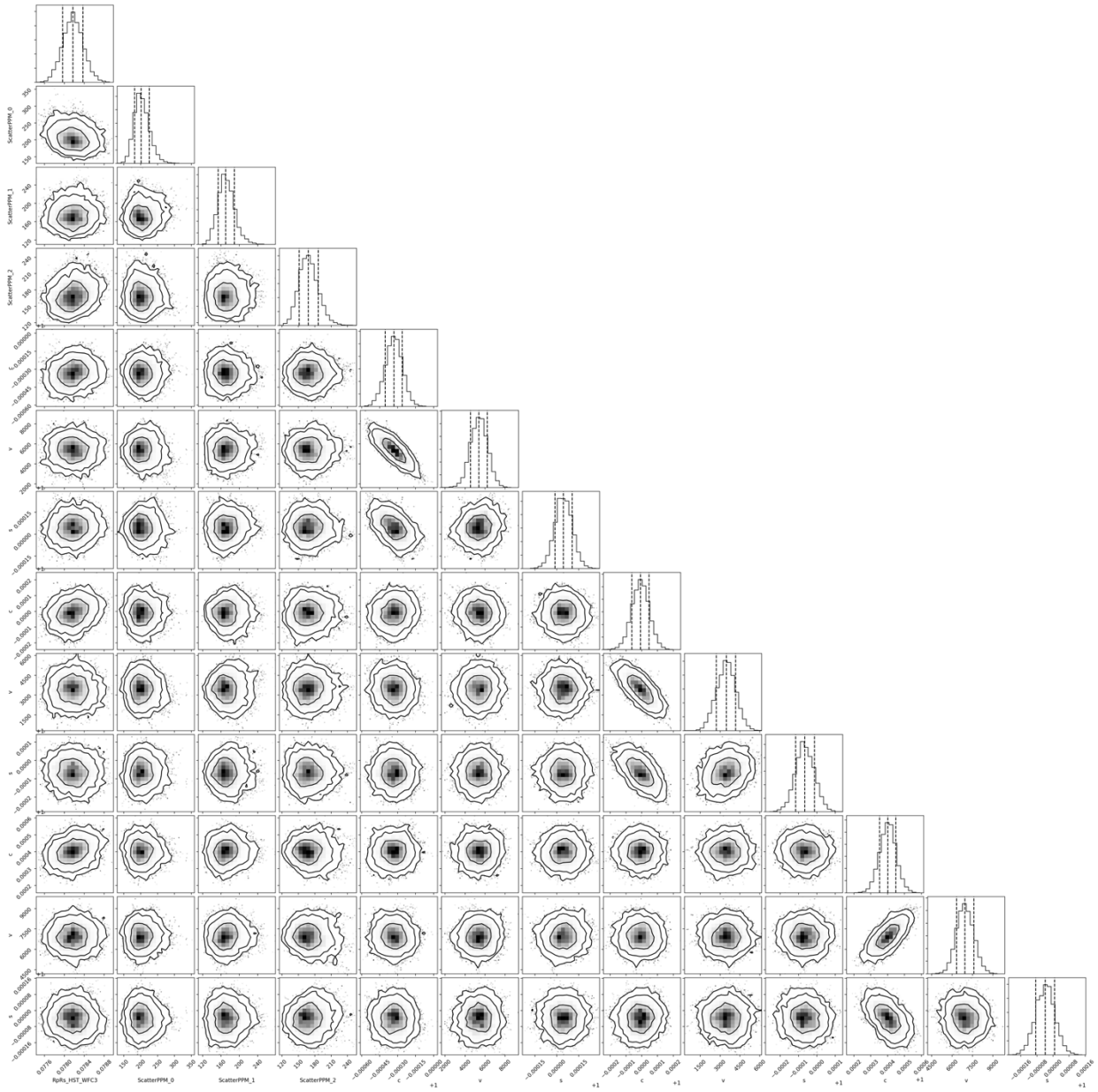


Supplementary Figure 14: Pairs plot showing the posterior distribution of the MCMC fitting parameters for the WFC3 spectral light curve fit. The panels on the diagonal show the marginalized posterior distribution for each fitting parameter. The 68% credible interval is marked by vertical dashed lines and quantified above the panel. The off-diagonal panels show the two-dimensional marginalized distribution for pairs of parameters, with the gray shading corresponding to the probability density and black contours indicating the 68% and 95% credible regions. Our instrument modeling results in no significant correlation between astrophysical transit depth (first column) and instrumental detrending parameters.

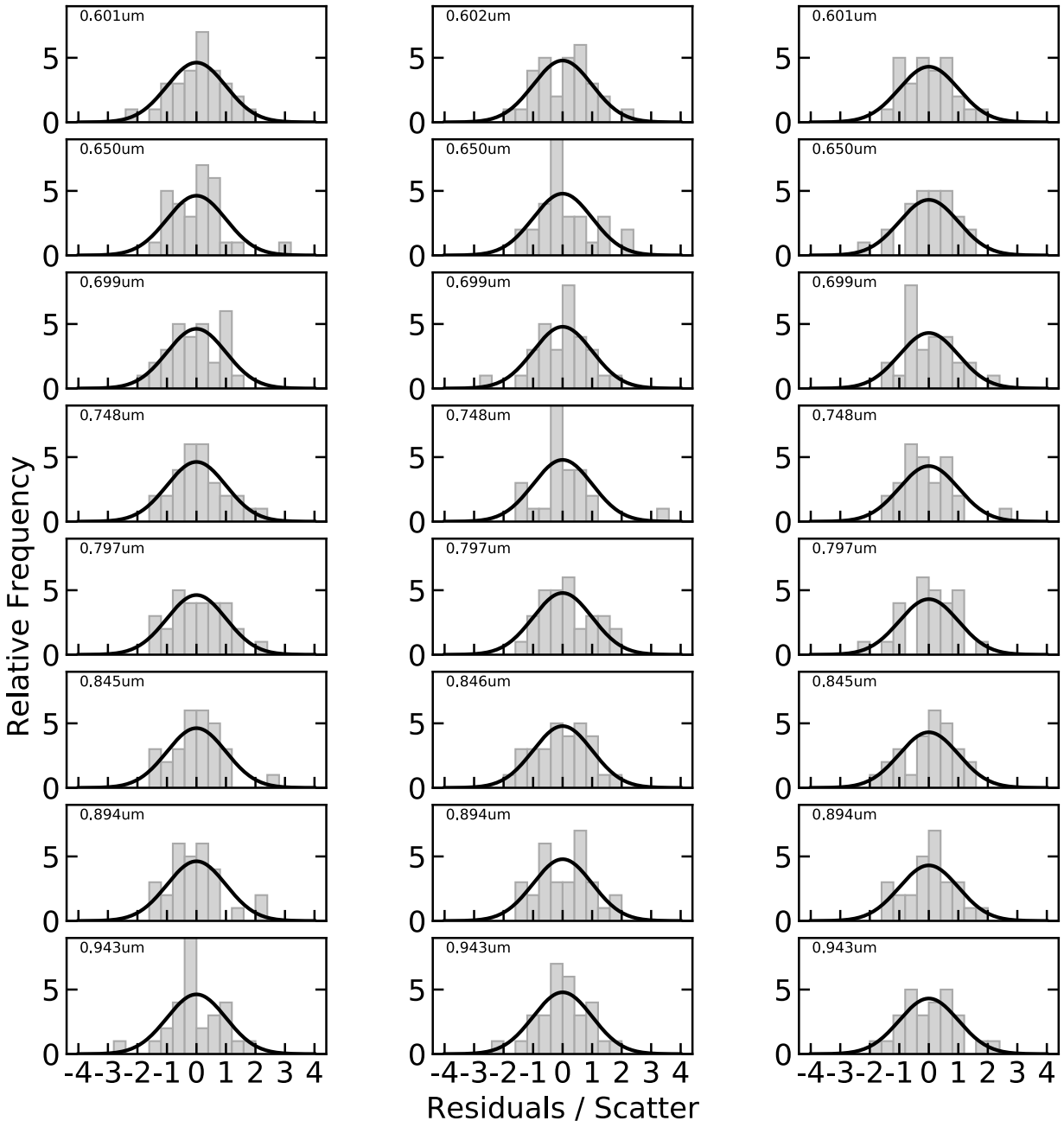


Supplementary Figure 15: Histograms of residuals from HST/STIS spectral light curve fits. This figure shows the histograms for each wavelength bin (rows) and each transit (columns) individually. Residuals are normalized by the maximum likelihood value of the scatter parameter for the respectively wavelength bin and transit. The histograms of the normalized residuals (gray bars) are compared to the normal distribution (black curve). Each histogram is made up of 29 data points leading to relatively poor sampling of each frequency distribution. All residuals combined are shown in Supplementary Figure 16. STIS residuals are consistent with a Gaussian distribution and the fitted scatter parameter is a conservative estimate of the scatter.

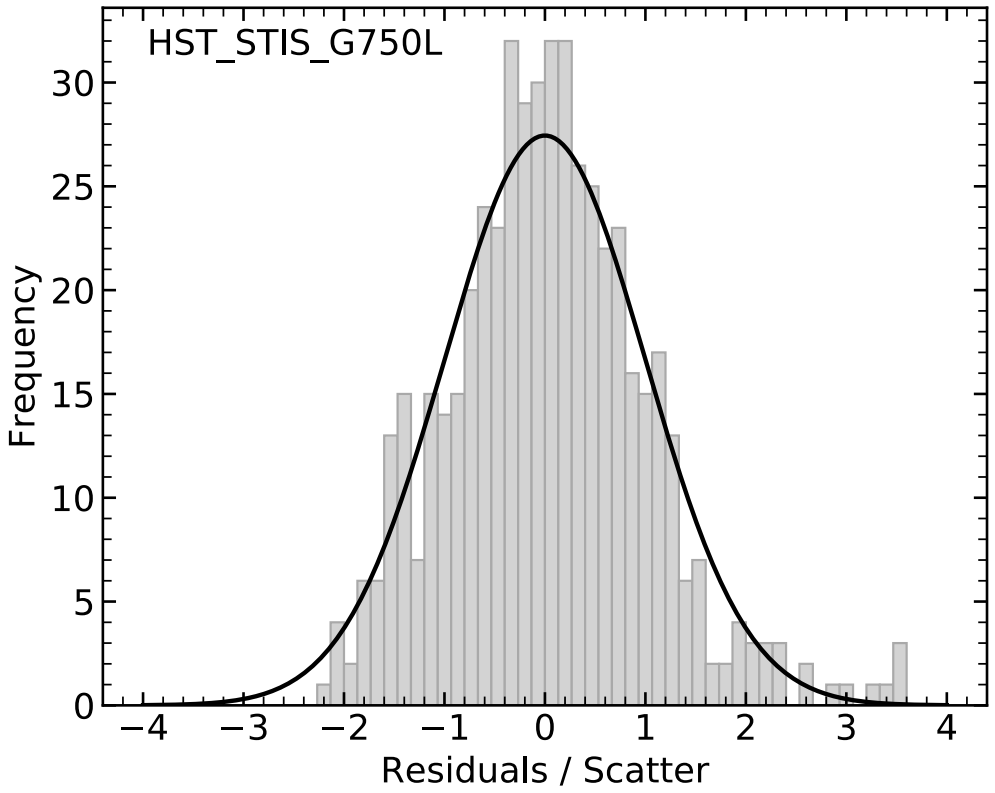


928

929 Supplementary Figure 16: Histograms of all residuals from STIS spectral light curve fits. This plot
930 combines the residuals from all panels in Supplementary Figure 15 in order to improve the number of
931 samples in the histogram. A distribution marginally narrower than the median of the scatter parameters is
932 found. We conclude that our Bayesian analysis of the STIS light curves conservatively estimated the error
933 bar as a result of the many detrending parameters needed to fit STIS light curves. This results in a
934 conservative estimate of the transit depth uncertainties. Note that a standard maximum likelihood method
935 would have found a smaller scatter because it would have estimated the scatter only based on the best fitting
936 (potentially overfitting) model.

937

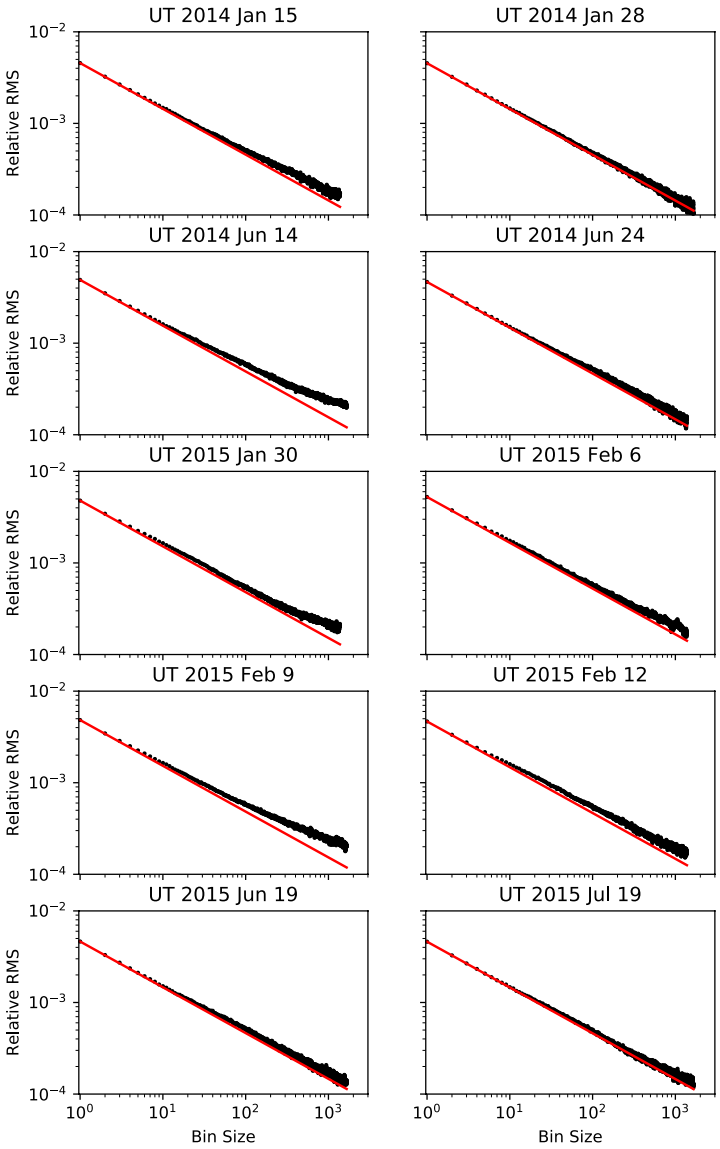


Supplementary Figure 16: Photometric scatter vs. the width of the binning interval for the ten Spitzer/IRAC 3.6um eclipses. The root-mean-square error of the systematics-corrected Spitzer data (black) follows closely the theoretical square-root scaling for uncorrelated white noise (red dashed line), even when combining up to 100 to 1000 data points to one bin.

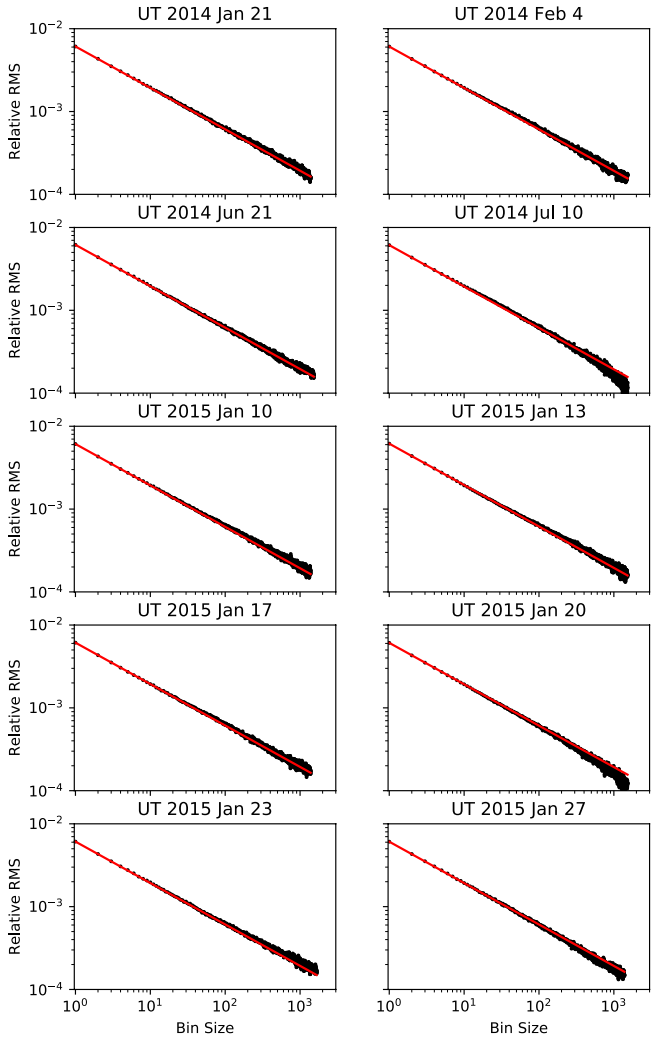


944

945 Supplementary Figure 17: Photometric scatter vs. the width of the binning interval for the ten Spitzer/IRAC
946 3.6μm eclipses. The root-mean-square error of the systematics-corrected Spitzer data (black) follows
947 closely the theoretical square-root scaling for uncorrelated white noise (red dashed line), even when
948 combining up to 100 to 1000 data points to one bin.

949

31. Bonfils, X. *et al.* A hot Uranus transiting the nearby M dwarf GJ 3470. Detected with HARPS velocimetry. Captured in transit with TRAPPIST photometry. *Astron. Astrophys.* **546**, A27 (2012).
32. Crossfield, I. J. M., Barman, T., Hansen, B. M. S. & Howard, A. W. Warm ice giant GJ 3470b: I. A flat transmission spectrum indicates a hazy, low-methane, and/or metal-rich atmosphere⋆. *Astron. Astrophys.* **559**, A33 (2013).
33. Dragomir, D. *et al.* Rayleigh Scattering in the Atmosphere of the Warm Exo-Neptune GJ 3470b. *Astrophys. J.* **814**, 102 (2015).
34. Biddle, L. I. *et al.* Warm ice giant GJ 3470b – II. Revised planetary and stellar parameters from optical to near-infrared transit photometry. *Mon. Not. R. Astron. Soc.* **443**, 1810–1820 (2014).
35. Deming, D. *et al.* Infrared Transmission Spectroscopy of the Exoplanets HD 209458b and XO-1b Using the Wide Field Camera-3 on the Hubble Space Telescope. *Astrophys. J.* **774**, 95 (2013).
36. Tsiaras, A. *et al.* A new approach to analysing HST spatial scans: the transmission spectrum of HD 209458b. (2015).
37. Tsiaras, A. *et al.* A Population Study of Gaseous Exoplanets. *Astron. J.* **155**, 156 (2018).
38. Demory, B.-O. *et al.* Spitzer Observations of GJ 3470 b: A Very Low-density Neptune-size Planet Orbiting a Metal-rich M Dwarf. *Astrophys. J.* **768**, 154 (2013).
39. Kammer, J. A. *et al.* Spitzer Secondary Eclipse Observations of Five Cool Gas Giant Planets and Empirical Trends in Cool Planet Emission Spectra. *Astrophys. J.* **810**, 118 (2015).
40. Knutson, H. A. *et al.* 3.6 and 4.5 μm Phase Curves and Evidence for Non-equilibrium Chemistry in the Atmosphere of Extrasolar Planet HD 189733b. *Astrophys. J.* **754**, 22 (2012).
41. Lewis, N. K. *et al.* Orbital Phase Variations of the Eccentric Giant Planet HAT-P-2b. *Astrophys. J.* **766**, 95 (2013).
42. Benneke, B. *et al.* Spitzer Observations Confirm and Rescue the Habitable-zone Super-Earth K2-18b for Future Characterization. *Astrophys. J.* **834**, 187 (2017).
43. Berta, Z. K. *et al.* THE FLAT TRANSMISSION SPECTRUM OF THE SUPER-EARTH GJ1214b FROM WIDE FIELD CAMERA 3 ON THE HUBBLE SPACE TELESCOPE. *Astrophys. J.* **747**, 35 (2012).
44. Sing, D. K. *et al.* Determining atmospheric conditions at the terminator of the hot-Jupiter HD209458b. *0803.1054* (2008). doi:doi:10.1086/590076
45. Nikolov, N. *et al.* Hubble Space Telescope hot Jupiter transmission spectral survey: a detection of Na and strong optical absorption in HAT-P-1b. *Mon. Not. R. Astron. Soc.* **437**, 46–66 (2014).
46. Sing, D. K. *et al.* A continuum from clear to cloudy hot-Jupiter exoplanets without primordial water depletion. *Nature* **529**, 59–62 (2016).
47. Wakeford, H. R. *et al.* HAT-P-26b: A Neptune-mass exoplanet with a well-constrained heavy element abundance. *Science* **356**, 628–631 (2017).
48. Lothringer, J. D. *et al.* An HST /STIS Optical Transmission Spectrum of Warm Neptune GJ 436b. *Astron. J.* **155**, 66 (2018).
49. Deming, D. *et al.* SPITZER SECONDARY ECLIPSES OF THE DENSE, MODESTLY-IRRADIATED, GIANT EXOPLANET HAT-P- USING PIXEL-LEVEL DECORRELATION. *Astrophys. J.* **805**, 132 (2015).
50. Kreidberg, L. batman: BAsic Transit Model cAlculatioN in Python. *Publ. Astron. Soc. Pac.* **127**, 1161 (2015).

51. Mandel, K. & Agol, E. Analytic Light Curves for Planetary Transit Searches. *Astrophys. J. Lett.* **580**, L171 (2002).
52. Husser, T.-O. *et al.* A new extensive library of PHOENIX stellar atmospheres and synthetic spectra. *Astron. Astrophys.* **553**, A6 (2013).
53. Parviainen, H. & Aigrain, S. ldtk: Limb Darkening Toolkit. *Mon. Not. R. Astron. Soc.* **453**, 3821–3826 (2015).
54. Demory, B.-O. *et al.* Spitzer Observations of GJ 3470 b: A Very Low-density Neptune-size Planet Orbiting a Metal-rich M Dwarf. *Astrophys. J.* **768**, 154 (2013).
55. Kosiarek, M. R. *et al.* Bright Opportunities for Atmospheric Characterization of Small Planets: Masses and Radii of K2-3 b, c, d and GJ3470 b from Radial Velocity Measurements and Spitzer Transits. *ArXiv181208241 Astro-Ph* (2018).
56. Foreman-Mackey, D., Hogg, D. W., Lang, D. & Goodman, J. emcee: The MCMC Hammer. *Publ. Astron. Soc. Pac.* **125**, 306–312 (2013).
57. Goodman, J. & Weare, J. Ensemble samplers with affine invariance. *Commun. Appl. Math. Comput. Sci.* **5**, 65–80 (2010).
58. Sing, D. K., Vidal-Madjar, A., Désert, J. -M., Lecavelier des Etangs, A. & Ballester, G. Hubble Space Telescope STIS Optical Transit Transmission Spectra of the Hot Jupiter HD 209458b. *Astrophys. J.* **686**, 658–666 (2008).
59. Dragomir, D. *et al.* Rayleigh Scattering in the Atmosphere of the Warm Exo-Neptune GJ 3470b. *Astrophys. J.* **814**, 102 (2015).
60. Fisher, C. & Heng, K. Retrieval analysis of 38 WFC3 transmission spectra and resolution of the normalization degeneracy. *Mon. Not. R. Astron. Soc.* **481**, 4698–4727 (2018).
61. Benneke, B. & Seager, S. ATMOSPHERIC RETRIEVAL FOR SUPER-EARTHS: UNIQUELY CONSTRAINING THE ATMOSPHERIC COMPOSITION WITH TRANSMISSION SPECTROSCOPY. *Astrophys. J.* **753**, 100 (2012).
62. Knutson, H. A., Benneke, B., Deming, D. & Homeier, D. A featureless transmission spectrum for the Neptune-mass exoplanet GJ 436b. *Nature* **505**, 66–68 (2014).
63. Benneke, B. Strict Upper Limits on the Carbon-to-Oxygen Ratios of Eight Hot Jupiters from Self-Consistent Atmospheric Retrieval. *ArXiv150407655 Astro-Ph* (2015).
64. Parmentier, V. & Guillot, T. A non-grey analytical model for irradiated atmospheres: I. Derivation. *Astron. Astrophys.* **562**, A133 (2014).
65. Line, M. R. *et al.* A Systematic Retrieval Analysis of Secondary Eclipse Spectra. I. A Comparison of Atmospheric Retrieval Techniques. *Astrophys. J.* **775**, 137 (2013).
66. Gao, P. & Benneke, B. Microphysics of KCl and ZnS Clouds on GJ 1214 b. *Astrophys. J.* **863**, 165 (2018).
67. Morley, C. V. *et al.* Quantitatively Assessing the Role of Clouds in the Transmission Spectrum of GJ 1214b. *Astrophys. J.* **775**, 33 (2013).
68. Morley, C. V. *et al.* Thermal Emission and Reflected Light Spectra of Super Earths with Flat Transmission Spectra. *Astrophys. J.* **815**, 110 (2015).
69. Line, M. R., Knutson, H., Deming, D., Wilkins, A. & Desert, J.-M. A Near-infrared Transmission Spectrum for the Warm Saturn HAT-P-12b. *Astrophys. J.* **778**, 183 (2013).
70. Tennyson, J. & Yurchenko, S. N. ExoMol: molecular line lists for exoplanet and other atmospheres. *Mon. Not. R. Astron. Soc.* **425**, 21–33 (2012).
71. Rothman, L. S. *et al.* HITEMP, the high-temperature molecular spectroscopic database. *J. Quant. Spectrosc. Radiat. Transf.* **111**, 2139–2150 (2010).

72. Swain, M. R., Line, M. R. & Deroo, P. ON THE DETECTION OF MOLECULES IN THE ATMOSPHERE OF HD 189733b USINGHSTNICMOS TRANSMISSION SPECTROSCOPY. *Astrophys. J.* **784**, 133 (2014).
73. Waldmann, I. P. *et al.* \textdollar$\lbrace$\textbackslashmathcal$\lbrace$T$\rbrace$$\rbrace$\textdollar-REx. II. RETRIEVAL OF EMISSION SPECTRA. *Astrophys. J.* **813**, 13 (2015).
74. Line, M. R. *et al.* No Thermal Inversion and a Solar Water Abundance for the Hot Jupiter HD 209458b from HST/WFC3 Spectroscopy. *Astron. J.* **152**, 203 (2016).
75. Moses, J. I. *et al.* Disequilibrium Carbon, Oxygen, and Nitrogen Chemistry in the Atmospheres of HD 189733b and HD 209458b. *Astrophys. J.* **737**, 15 (2011).
76. Moses, J. I. *et al.* On the Composition of Young, Directly Imaged Giant Planets. *ArXiv160808643 Astro-Ph* (2016).